FEDSM-ICNMM2010-' $* , +

LES OF THE FLOW AROUND A GENERIC WHEEL IN A WHEELHOUSE

Siniša Krajnović[*]
Division of Fluid Dynamics,
Department of Applied Mechanics,
Chalmers University Of Technology,
SE-412 96 Göteborg, Sweden
Email: sinisa@chalmers.se
http://www.tfd.chalmers.se/~sinisa

Sasan Sarmast

Division of Fluid Dynamics,
Department of Applied Mechanics,
Chalmers University Of Technology,
SE-412 96 Göteborg, Sweden

Branislav Basara

AVL List GmbH, Advanced Simulation Technologies,
Graz, Austria

ABSTRACT

The flow around generic wheels in wheel housings used in previous experimental investigations is studied using large eddy simulations. A comparison is given here of the results of the simulations with existing experimental data and previous qualitative results of RANS simulations. Both instantaneous and time averaged flows are described, showing agreement with previous knowledge and adding new insight in flow physics. Two different widths of the wheel housing are used in the simulations, and their influence on the flows is studied. The present work shows that the width of the wheel housing has an influence on flows on both the inside and the outside of the wheel.

INTRODUCTION

Wheels and wheelhouses have a large influence on the aerodynamic performance of ground vehicles. Their contribution to drag is around $30 - 40\%$ (1) and they are responsible for much of the mud, water and snow deposition on the ve-hicle. Furthermore, the design of the wheelhouse with the wheel inside has an influence on water splashes in wet road conditions on surrounding vehicles, thus affecting traffic safety. The flow around isolated wheels has received much attention by the research community (2; 3; 4; 5; 6). Although a physical description of the instantaneous flow around isolated wheels is yet not available, the time-averaged flow is fairly well understood. The placement of wheels on vehicles has a great influence on the wheel flow for two reasons. First, the flow underneath a ground vehicle spreads out-ward to the sides (7). This leads to a flow approaching a wheel at an angle of yaw. As a result of the yawed approaching flow, the flow separates on the outside of the wheels. The position of the separation depends on the value of the yawing angle (e.g. 15% is reported in the literature (8) for passenger cars) and, with the position of separation, the size of the wheels' wake is determined, with all its influence on the vehicle, as well as on splash formation on wet roads.

Wheels are always placed in wheel housings which further complicates the flow around wheels.

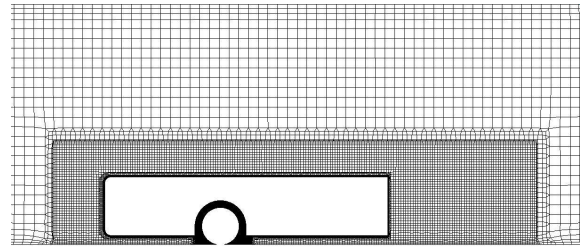[*]Address all correspondence to this author.
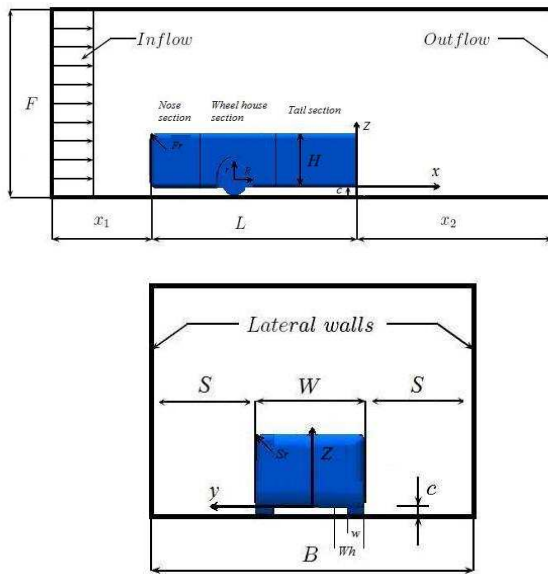
Figure 1. Schematic representation of the computational domain with vehicle body. Left: view side ; right: front view. Values of geometric parameters are given in Table 1

Figure 2. Details of the computational grid showing a) plane $y/H = 1.66$; b) plane $z/H = 0.2$; and c) perspective view of the wheelhouse

No complete physical model of the flow around a wheel within a wheel housing yet exists, and this is the motivation for the present work.
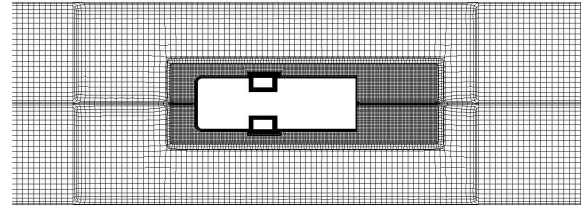
There is no doubt that the understanding of the complicated interaction of wheels with the wheel housing is crucial for understanding their influence on vehicles' drag and water and dirt deposition. A wheel housing often has the shape of a half-cylindrical cavity with its outer side open (but partly shielded by the wheel). The rotation of the wheel and motion of the vehicle lead the air and water swirls into the wheel housing, which are then (due to yawed flow) partly convected and partly sucked out to the outer side owing to the negative pressure in the wake on the wheels outer side. This flow mechanism has a great influence on the drag, directional stability, mud/water deposition and water splashes. The present work uses large-eddy simulation to study the flow of an idealized wheel in a wheel housing with the aim of increasing the knowledge about this flow.
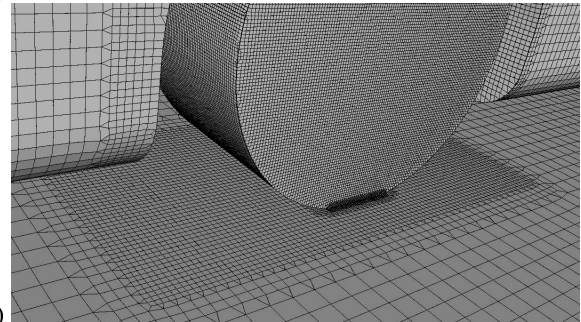
Previous work

Investigations of flows around wheels in wheelhouses and the flows' effects on their aerodynamic performance have been studied using both experimental and numerical techniques. For example, Oswald and Browne (9) measured the flow field around a wheel within a wheelhouse cavity using a single axis hot-wire probe for velocity and turbulence measurements, and the local flow direction was determined using a tuft grid fitted around the front wheel. Cogotti (2) studied the change of drag and lift of idealized bodies when wheelhouses and wheels were added. One observation in his study was that the increase in drag and lift of the teardrop body from adding wheels was reduced by keeping the wheelhouse volume as small as possible. Fabianic (10) and Fabianic and George (11) studied the influence of various wheelhouse parameters on the flow around a shrouded wheel. One of these wheelhouse parameters was the wheelhouse volume, and its influence on the flow will also be studied in the present paper. Their flow visualizations showed that the flow was highly unsteady, indicating that, if modeled, the numerical technique must be capable of dealing with such an unsteady flow with a wide spec-

trum of turbulent scales. This is the motivation in the present work for using large-eddy simulations capable of dealing with massively separated unsteady flows. Both aerodynamic forces and the surface pressure inside the wheelhouse were measured in (10) and (11). However, the accuracy of the measured data was low due to problems in controlling the experimental set-up.

The geometry studied in (10) (as well as a few other similar geometries) was recently studied numerically by Regert and Lajos (12), who used Reynolds-averaged Navier Stokes equations both in their natural steady (RANS) and unsteady (URANS) formulations. Because of unreliable experimental data (13) from (10), not very much comparison was made with the experiments. A new description of the time-averaged flow structures was presented, however. URANS simulations in (12) resulted in a quasi steady flow and only results of steady RANS simulations were presented. Axon et al. (14) used RANS simulations with the RNG $k - \varepsilon$ turbulence model to predict the flow around a wheel in a wheelhouse cavity. They compared the aerodynamic forces and the pressure coefficients on the internal faces of the cavity. According to the authors, good qualitative agreement of the simulation results with the experimental data was obtained. Skea et al. (15) used steady RANS simulations with RNG $k - \varepsilon$ turbulence model to simulate the flow around the wheel in a wheelhouse similar to that in (10) and in the present work. Although their simulation predicted the main features of the flow, the separation and reattachments indicated by a change of pressure coefficients on the surface were not accurately predicted. The reason for this failure in flow prediction was assumed to be that the flow was transient at the rear of the wheel and under the wheel arch. Washle (16) investigated the aerodynamic influence of the rotating wheel on both a simplified vehicle model and a series production car. He used both the experimental techniques of force measurements and LDV as well as RANS simulations. The result of his study was that the rotation of the wheel is important for the flow in and around a wheelhouse and its influence on vehicles' aerodynamic performance.

DESCRIPTION OF THE MODEL

The vehicle geometry used in present work is the one used in experimental work of Fabijanic (10). In his experimental study, Fabijanic (10) studied the influence of adding the wheelhouse and wheels to the basic geometry. He furthermore investigated the influence of the wheelhouse vol-

ume on the aerodynamic coefficients and pressure distribution around wheels.

The basic form of the vehicle shown in Fig. 1 is a rectangular box with a dimension of H height and W width resulting in a model aspect ratio (AR), defined as model width divided by model height of 1.5. The model consists of rear, nose and wheel-well sections; the nose, wheelhouse and rear sections have 95.8, 177.8 and 254 mm. Struts and holdings are used in the experiments by Fabijanic (10) but are not included in present simulations due to their unknown positions. Two different volumes of the wheelhouse equal to 2 (Case 1) and 2.8 (Case 2) volumes of the wheel are used in the present work. The Reynolds number based on the inlet velocity of 30 m/s and the wheel diameter was 1.6×10^5. The wheels rotated at the rotating velocity of 783.2 rad/s, which corresponds to the ground velocity equal to the inlet velocity of the air.

The computational domain with the vehicle model is shown in Fig. 1. Its cross section is identical to that of the Cornell University Upson low noise wind tunnel where the experiments were performed. However, the length was adjusted and the upstream length in the simulation is $8H$ (H being the height of the model) and the distance behind the model to the outlet is $21H$, in agreement with practice for this kind of simulation established in previous work by Krajnović et al. (7; 17; 18). The velocity profile at the inlet used in the experiments was uniform within 1%, and the turbulence level was less than 0.6%.

1 LES Governing Equations

The governing LES equations are the incompressible Navier-Stokes and the continuity equations filtered with the implicit spatial filter of characteristic width Δ (Δ is the grid resolution in this work):
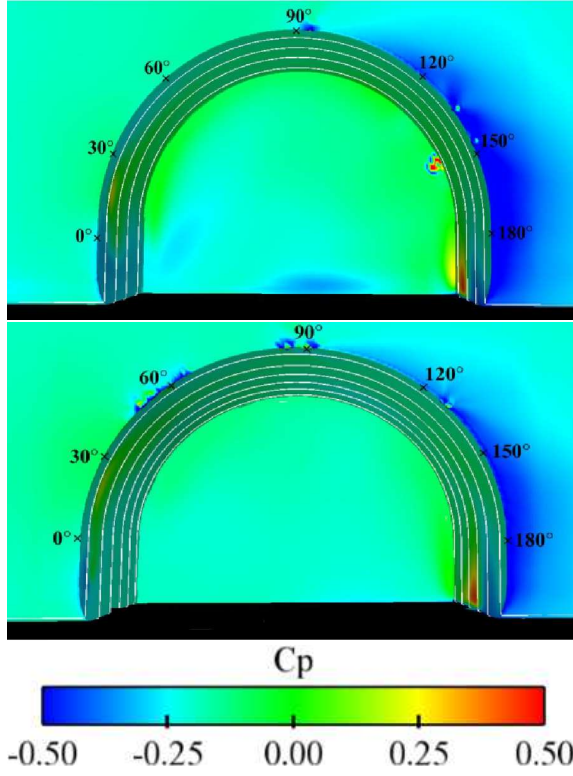
$$\frac{\partial \bar{u}_i}{\partial t} + \frac{\partial}{\partial x_j}\left(\bar{u}_i \bar{u}_j\right) = -\frac{1}{\rho}\frac{\partial \bar{p}}{\partial x_i} + \nu \frac{\partial^2 \bar{u}_i}{\partial x_j \partial x_j} - \frac{\partial \tau_{ij}}{\partial x_j} \quad (1)$$

and

$$\frac{\partial \bar{u}_i}{\partial x_i} = 0. \quad (2)$$

Here, $\bar{u}_i$ and $\bar{p}_i$ are the resolved velocity and pressure, respectively, and the bar over the variable denotes filtering.

The influence of the small scales of the turbulence on the large energy carrying scales in Eq. (1)

Figure 3. Wheelhouse side region pressure distribution C_P and wheelhouse inner wheelhouse arch region details a)Case 1, Width of inner wheelhouse arch region is divided into four rows b) Case 2 , Width of inner wheelhouse arch region is divided into six rows.

appears in the SGS stress tensor, $\tau_{ij} = \overline{u_i u_j} - \bar{u}_i \bar{u}_j$. The algebraic eddy viscosity model originally proposed by Smagorinsky (19) is used in this paper for its simplicity and low computational cost. The Smagorinsky model represents the anisotropic part of the SGS stress tensor, τ_{ij}, as:
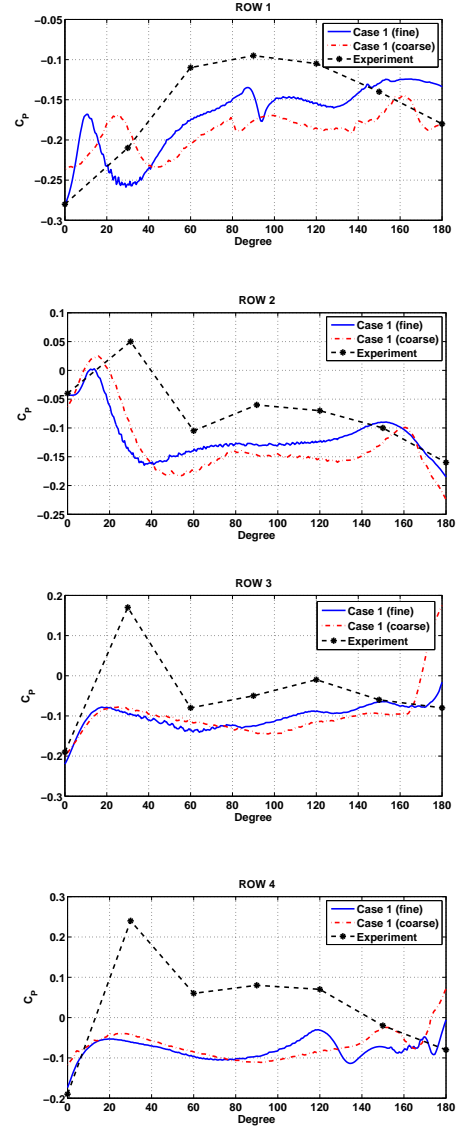
$$\tau_{ij} - \frac{1}{3}\delta_{ij}\tau_{kk} = -2\nu_{sgs}\bar{S}_{ij} \qquad (3)$$

where $\nu_{sgs} = (C_s f \Delta)^2 |\bar{S}|$ is the SGS viscosity,

$$\bar{S}_{ij} = \frac{1}{2}\left(\frac{\partial \bar{u}_i}{\partial x_j} + \frac{\partial \bar{u}_j}{\partial x_i}\right) \qquad (4)$$

is the resolved rate-of-strain tensor and $|\bar{S}| = \left(2\bar{S}_{ij}\bar{S}_{ij}\right)^{\frac{1}{2}}$. f in the expression for the SGS viscosity is the van Driest damping function

$$f = 1 - \exp\left(\frac{n^+}{25}\right). \qquad (5)$$

Figure 4. Wheelhouses' arch pressure coefficient distribution of Case 1, fine and coarse meshes and experiment

where n is the wall normal distance. Using this damping function, wall effects are partially taken into account by 'damping' length scale $l = C_s \Delta$ near the walls. The value of $C_s = 0.1$ previously used for bluff-body flows (20) and flow around a simplified bus (7) and generic car called the Ahmed body (17) is used in this work. The filter width, Δ, is defined in this work as $\Delta = (\Delta_1 \Delta_2 \Delta_3)^{1/3}$, where Δ_i are the computational cell sizes in three coordinate directions.

4
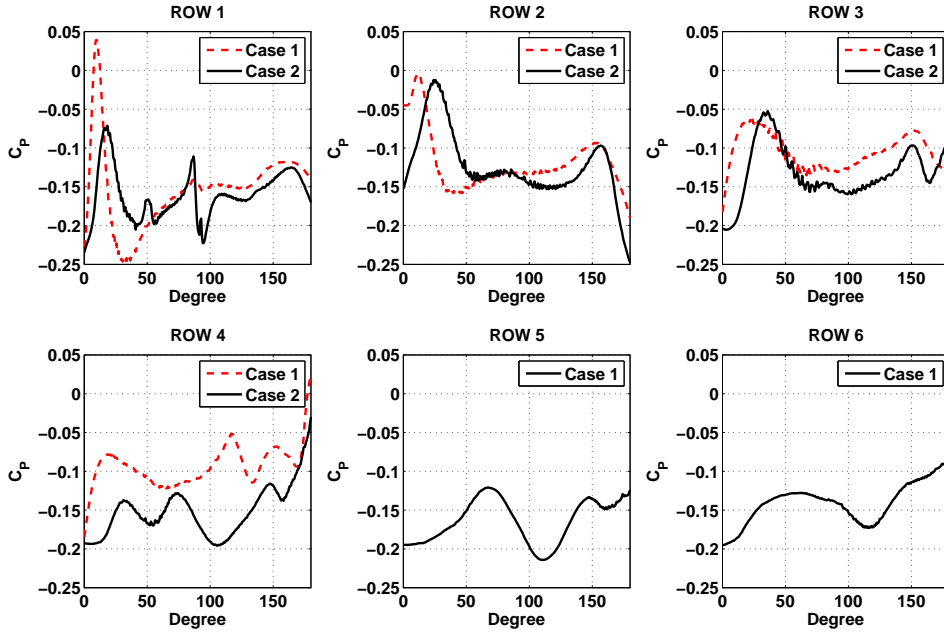
Figure 5. Wheelhouse arch pressure coefficient C_P distribution four rows in Fig. 3 (a) for Case 1 and six rows in Fig. 3 (b) for Case 2

1.1 Numerical Method

Equations (1) and (2) are discretized using a 3D finite volume method for solving the incompressible Navier-Stokes equations using a collocated grid arrangement. Both convective and viscous plus sub-grid fluxes are approximated by a blend of 95% central differences of second-order accuracy and of 5% upwind differences. The time integration is done using the second-order accurate three time level scheme.

2 Spatial and temporal resolution

A grid refinement study using two different computational grids was done for each of the three cases, the base case, Case 1 and Case 2, in order to assess numerical accuracy. The total number of computational points insreased from 4.4 to 8.5 milion nodes for Case 1 and from 4.6 to 12.5 million nodes for Case 2, between the coarse and the fine computational grids, respectively. Computational grids were made in FAME Hexa of AVL and were hexa dominated, as seen in Fig. 2. As the objective was to study the flow in the wheelhouse, the largest number of computational cells were placed in the wheelhouses. For example, around 82% and 80% of the computational cells were placed in the wheelhouse in Cases 1 and 2, respectively, in the

fine computational grids.

The fine computational grid (containing 12.5 million nodes) had a wall normal resolution of $n^+ < 0.9$, $9 < \Delta s^+ < 11$ in the streamwise direction and $9 < \Delta l^+ < 11$ in the direction parallel to the surface of the body and normal to the streamwise direction (the mean Δl^+ is around 10). Here, $\Delta n^+ = \Delta n \langle u_\tau \rangle_t / \nu$, $\Delta s^+ = \Delta s \langle u_\tau \rangle_t / \nu$, $\Delta l^+ = \Delta l \langle u_\tau \rangle_t / \nu$ and $\langle u_\tau \rangle_t$ is the time-averaged friction velocity. The time step was 5×10^{-4}, giving a maximum CFL number of approximately 1. All asimulations were first run during the non dimensional time of $tU_\infty / H = 144$ (1,220 time steps) which was found sufficient for flow to become fully developed. Afterwards, the flow was averaged during an averaging time of $tU_\infty / H = 283.5$ (2,400 time steps).

Numerical Accuracy

Numerical accuracy was checked by using two different computational grids for each set-up. Figure 4 shows a comparison of the surface pressure coefficients for Case 1 along four curves on the inside of the wheelhouse shown in Fig. 3. Row 1 is closest to the forward outboard edge of the wheel-well and row 4 is the closest to the inward of the wheel-well. Both computational grids produce similar results, proving that the resolution is
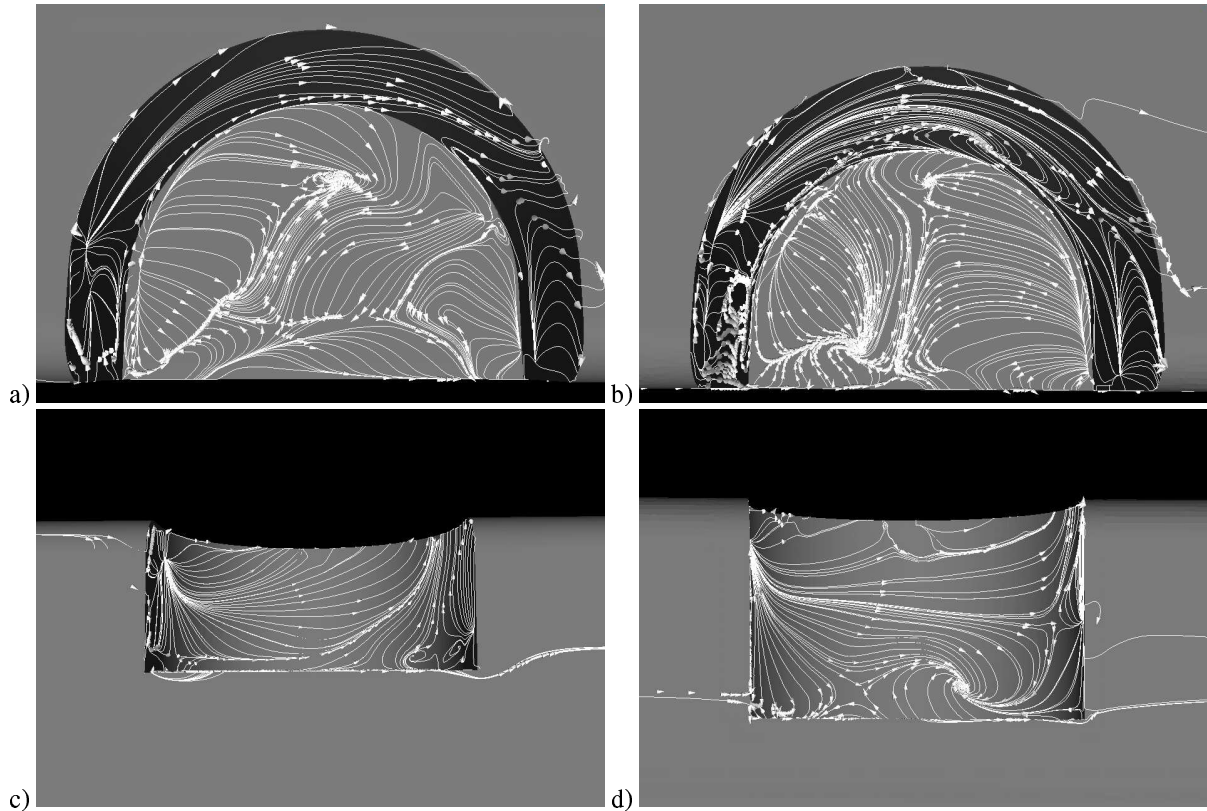
Figure 6. Time-averaged trace lines and velocity vectors projected on the surface of the wheelhouse showing surface flow patterns. Side views of a) Case 1 and b) Case 2. View from below of c) Case 1 and d) Case 2

sufficient for an LES. An additional comparison of the results between different computational grids is presented in Table 3, where drag and lift coefficients are compared. Case 2 requires more computational grids in the wheel well due to the larger volume. This is why the difference in drag coefficient between the two grids is around 11% (Table 3). All other differences in results between the two grids are small.

2.1 Comparison with the experiments

The comparison of the LES results was made with the existing surface pressure data and drag coefficients. Figure 4 shows comparisons of four C_p profiles along the inner side of the wheelhouse. The present LES simulations predict the pressure distribution in the wheelhouse to be different from that measured in experiments by Fabianic (10). Regert and Lajos (12) did not present the pressure distribution results of their RANS simulations, and it is not clear what is the reason for the discrepancy between the present LES results and the experimental data. Keeping in mind the similarity in the results for Case 1 between the two differ-

ent grids (Fig. 4) and the very fine spatial resolution in the wheelhouse, we are willing to believe that there is some discrepancy between the experimental and numerical set-ups not known to the authors. A similar observation was reported in (12), who documented the discrepancy in the numerical and computational set-ups due to a lack of accurate data about the experimental arrangement. Comparisons of the aerodynamic coefficients for the wheel are shown in Table 4. Although the difference between the LES coefficients and the experimental data for e.g. the drag coefficient is about 29% and 22% for Case 1 and Case 2, respectively, the experimental uncertainties are very large. Fabianic reported uncertainties for wheels C_D and C_L of ± 0.0087 and ± 0.007, respectively. This corresponds to uncertainties of 23% and 35% in drag and lift, respectively, for Case 1. Similar uncertainties for the complete vehicle in (10) were ± 0.018 for both the drag and the lift coefficients. As the absolute values for the total aerodynamic coefficients were not reported in (10), we can only relate the uncertainties to the LES values. As seen in Table 4, the uncertainties reported in (10) cor-

6
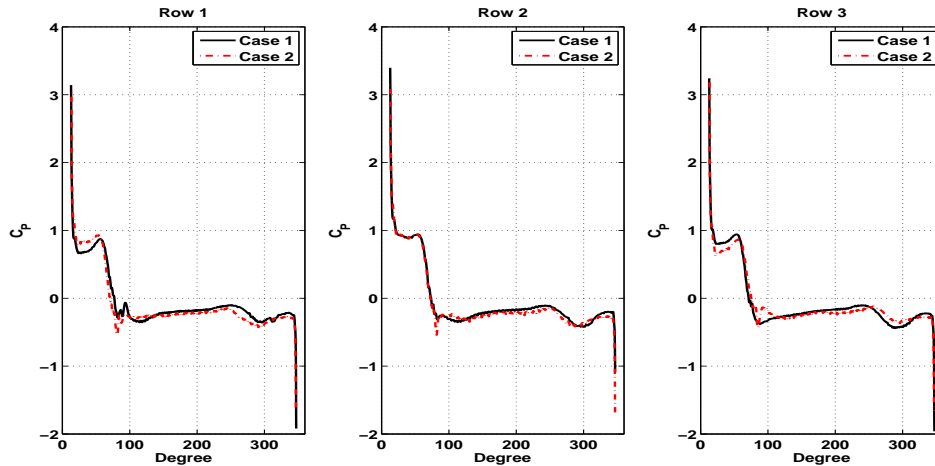
Figure 7. Wheel pressure coefficient distribution along three rows. The width of the wheelhouse is divided into three rows. Row 2 shows the wheel pressure distribution at the wheels' centerline.

respond to 5% and 37% of the LES drag and lift coefficients, respectively. Thus, the comparison of the present LES results with the experimental data, such as that of ΔC_D in Table 2, only has the purpose of documenting the differences between the LES results and the experimental data. The poor agreement between the two does not prove the wrongness of the simulation but, as noted in (12), shows a plausible difference in the set-ups.

2.2 Influence of the wheel depth

Figure 5 shows a comparison of the pressure coefficient along the curves in the inside of the wheel-well. The location of the curves is given in Fig. 3. The C_p profiles have approximately the same amplitudes at rows 1-3, after which (rows 4-6). The pressure decreases for Case 2 because of the wider wheel-well. This shows that the pressure picture in the flow region around the wheel is not influenced a great deal by the width of the wheel-well as long as the position of the wheel is the same in both cases with respect to the outer side of the body. One interesting observation is that the flow on the inner side of the wheel-well separates later in Case 2, indicated here by a later C_p peak. This is also visible in the trace lines shown in Fig. 6.

The pressure coefficient on the surface of the wheel at the lateral position of rows 1-3 on the wheel-well is shown in Fig. 7. Similar to the pressure picture on the wheel-well, no great difference in surface pressure is visible between the two cases.

2.3 Time-averaged flow structures

Figure 9 shows streamlines projected onto several x and y planes to illustrate the time-averaged coherent structures in the flow in Case 1. A sketch of the extracted flow features is shown in Fig. 8. The flow entering the wheelhouse from below forms first vortex H, which has an axis parallel with that of the wheel. In addition to the presentation of the vortex by means of streamlines and vortex cores in Fig.9. Figure 6. shows its imprint on the wheel-well with trace lines. Vortex H seems to continue into vortex C along the outer arch edge. Three other vortices, A, S and B, were found above the upper part of the wheel, in agreement with the findings of Regert and Lajos (12). Four vortices, R, R_1, L and L_1, were detected around the lower part of the wheel. All of these structures except R_1 and L_1, which are a new discovery in the present work are in agreement with those found in (12). The influence of the width of the wheelhouse on the time-averaged flow structures is presented in Fig. 11 using an isosurface of the low pressure and streamlines projected on several x planes. This figure shows that the width of the wheelhouse is a parameter that influences the position and strength of the vortices surrounding the wheel. This is particularly the case on inner side of the wheelhouse.

Figures 11 and 12 compare one velocity plane in the streamwise direction and another parallel with the outer lateral side of the wheel, respectively. These two pictures show that the wheelhouse width has an influence on the position and strength of vortex L. The size and position of vortex E seem not to be greatly affected by the change

7

Table 1. Values for the model and computational tunnel characteristic parameters

WindTunnel		
B	500	mm
F	750	mm
S	154.75	mm
x_1	8(H+c)=113.4	mm
x_2	21(H+c)=2977.8	mm
$B \times F$	0.375	mm^2
CarBasic		
W	190.5	mm
H	127	mm
L	591.1	mm
rs	12.7	mm
rf	25.4	mm
$W \times H$	0.0269	mm^2
wheelhouse		
w	36.2	mm
wh_{CASE1}	50.5	mm
wh_{CASE2}	70.4	mm
r	38.3	mm
R	52.3	mm
c	16.8	mm

Table 2. Results from experimental data and CFD for the modified vehicle

Aerodynamic Coefficients	ΔC_D	
	LES	Exp.
Case 1	0.113	0.11
Difference	3%	
Case 2	0.138	0.123
Difference	12%	

in the widths of the wheelhouse (Fig. 11).

## 2.4 Instantaneous flow structures

Instantaneous flow structures are visualized using a second invariant of the velocity gradient Q in Fig. 13. Although the slow structures are very

Table 3. Results from coarse and fine computational grids for the basic vehicle

Aerodynamic coefficients	C_D	C_L
Case 1 fine	0.3767	-0.0493
Case 1 coarse	0.3766	-0.0473
Difference	0.01%	6%
Case 2 fine	0.4242	-0.0454
Case 2 coarse	0.3757	-0.0469
Difference	11%	3%

**Table 4.** Results from experiment and CFD for the basic vehicle

Wheels' Aerodynamic Coefficients	C_D
Case 1	0.0266
Experiment	0.0375
Difference	29%
Case 2	0.0322
Experiment	0.0415
Difference	22%
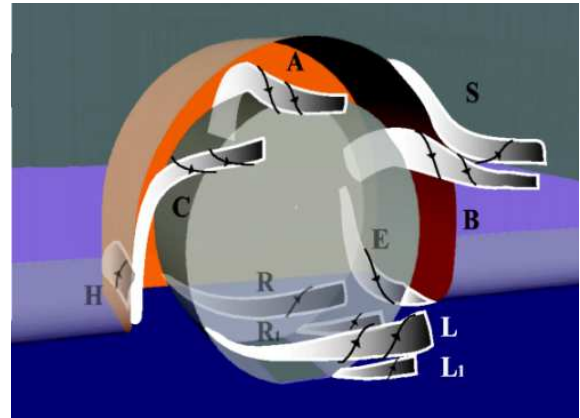
Figure 8. Vortex skeleton schematic model

different from those found in the time-averaged flow, the concentration of the coherent structures is greatest at the location of the time-averaged structures (denoted with letters in Fig. 13). One observation of extremely complex and fine scale streaky flow structures can be made from this figure. Furthermore, as seen in Fig. 14, the flow structures change over time. The instantaneous structures
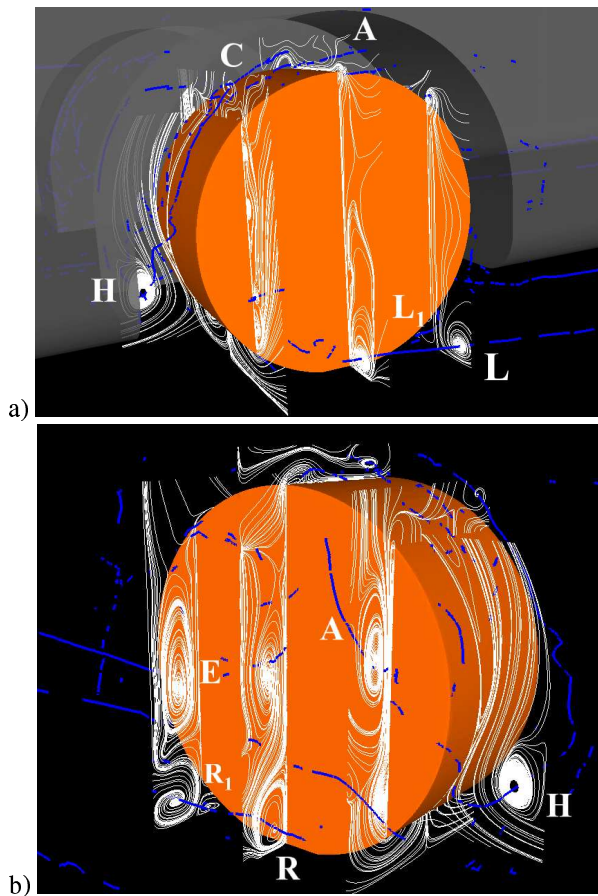
Figure 9. Vortex cores and time-averaged streamlines projected into different horizontal planes showing the time-averaged flow structure around the wheel inside the wheelhouse. The distance between each trace line plane field is $1/3$ the wheel diameter. a) Side view and b) Inside view

that contribute to the time-averaged vortex L seem to be enclosed in the confined region of the time-averaged vortex L. However, even these structures are convected downstream over time (Fig. 14).

Another interesting observation is the difference in the size and shape of the instantaneous structures between Cases 1 and 2. For example, the hairpin-like vorices forming the time-averaged vortex L are wider in Case 2 than in Case 1, as shown in Figs. 14 and 15.
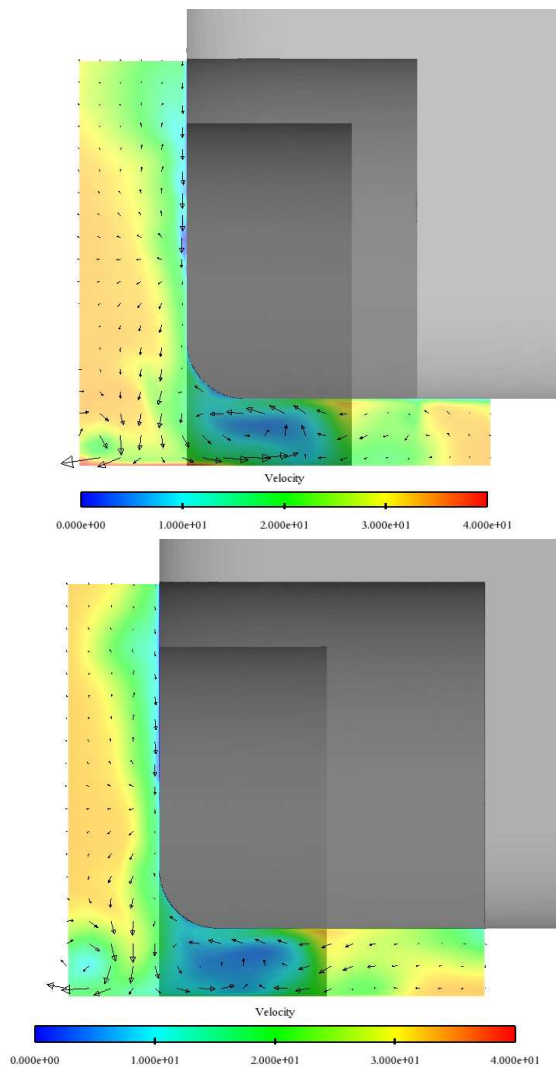
ACKNOWLEDGMENT
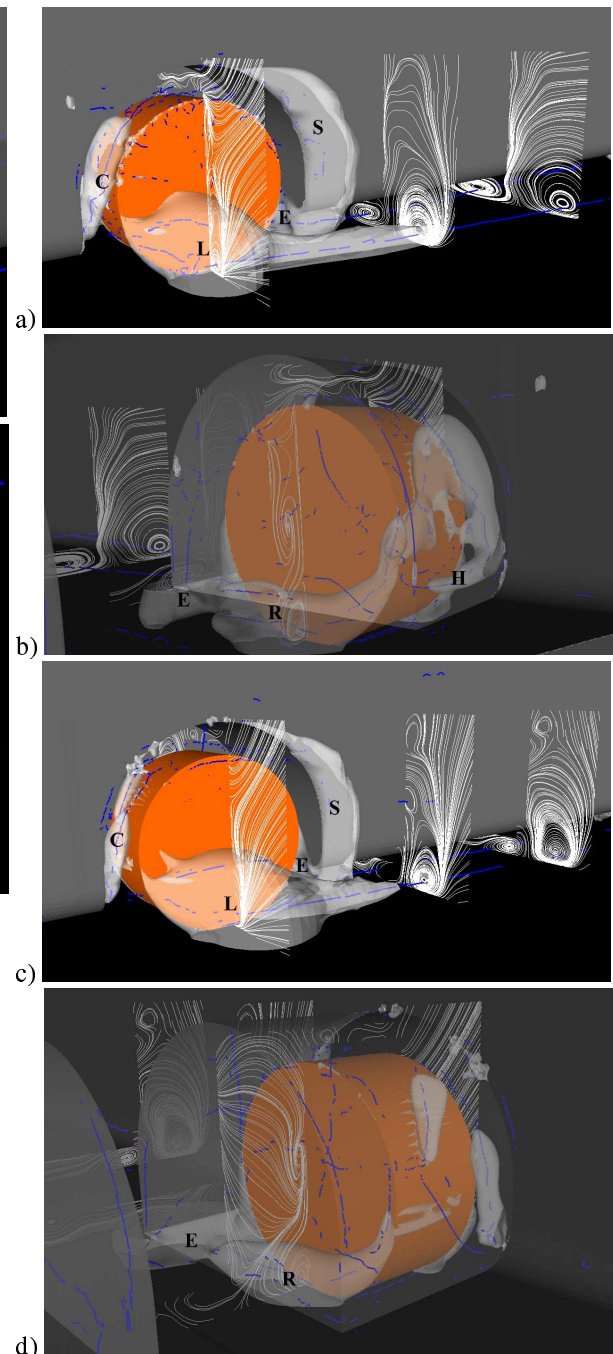
Figure 10. Iso-surface of pressure. $P = 1.0116$ Bar a) Case 1, side view, b) Case 2, side view c) Case 1, inside view and d) Case 2, snside view
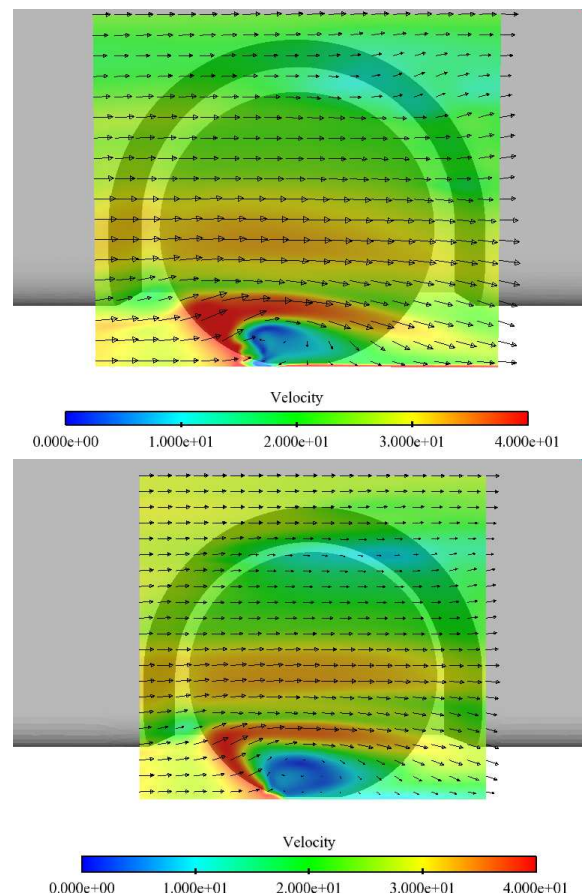
REFERENCES

[1] Elofsson, P., and Bannister, M., 2002. "Drag reduction mechanisms due to moving ground

Figure 11. Velocity fields in plane *x* which is 10 mm behind the wheel for a) Case 1 and b) Case 2.

Figure 12. Velocity fields in plane *y* which is 5 mm away from the whells' outer plane for a) Case 1 and b) Case 2.

and wheel rotation in passenger cars". In SAE Paper 2002-01-0531.

[2] Cogotti, A., 1983. "Aerodynamic characteristics of car wheels. in technological advances in vehicle design series". In SP3 Impact of Aerodynamics on Vehicle Design, International Journal of Vehicle Design, pp. 173–196.

[3] Mears, A. P., Crossland, S. C., and Dominy, R. G., 2004. "An investigation into the flowfield about an exposed racing wheel". In SAE 2004 World Congress.

[4] Wäschle, A., Cyr, S., Kuthada, T., and Wiedemann, J., 2004. "Flow around an isolated wheel - experimental and numerical comparison of two cfd codes". In SAE 2004 World Congress.

[5] Saddington, A. J., Knowles, R. D., and Knowles, K., 2007. "Laser doppler anemometry measurements in the near-wake of an isolated formula one wheel". *Experiments in Fluids*, **42**, pp. 671–681.

[6] McManus, J., and Zhang, X., 2006. "A computational study of the flow around an isolated wheel in contact with the ground". *ASME: Journal of Fluids Engineering*, **128**, pp. 520–530.

[7] Krajnović, S., and Davidson, L., 2003. "Numerical study of the flow around the bus-shaped body". *ASME: Journal of Fluids Engineering*, **125**, pp. 500–509.

[8] Wiedemann, J., 1996. "The influence of ground simulation and wheel rotation on aerodynamic drag optimization - potential for reducing fuel consumption.". In SAE paper 960672.

[9] Oswald, L. J., and Browne, A. L., 1981. "The
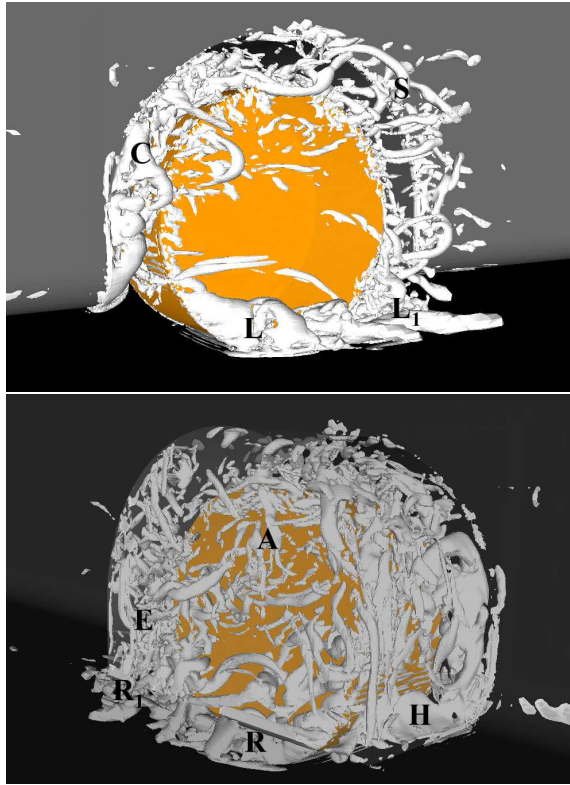
Figure 13. Iso-surface of the second invariant of the velocity gradient tensor $Q = 6 \times 10^6$. (a) Side view and (b) inside view

airflow field around and operating tire and its effects on tire power loss". In Technical Report 810166.

[10] Fabijanic, J., 1996. "An experimental investigation of wheel-well flows". In SAE Paper 960901.

[11] Fabianic, J., and George, A. R., 1996. "An experimental investigation of the aerodynamics of automobile wheel wells". In Technical Report 962475, AIAA.

[12] Regert, T., and Lajos, T., 2007. "Description of flow field in the wheelhouses of cars". *Int. J. Heat and Fluid Flow, 28*, pp. 616–629.

[13] Regert, T., 2009. Private communication. Budapest University of Technology and Economics, Budapest, Hungary.

[14] L. Axon, K. G., and Howell, J., 1999. "The influence of ground condition on the flow around a wheel located within a wheelhouse cavity". In SAE Paper 1999-01-0806.

[15] A. F. Skea, P. R. B., and Qiao, J., 2000. "Cfd simulations and experimental measurements of the flow over a rotating wheel in a wheel arch,". In SAE Paper 2000-01-0487.

[16] Waschle, A., 2007. "The influence of rotating wheels on vehicle aerodynamics- numerical and experimental investigations". In SAE Paper 2007-01-0107.

[17] Krajnović, S., and Davidson, L., 2005. "Flow around a simplified car, part 1: Large eddy simulation". *ASME: Journal of Fluids Engineering, 127*, pp. 907–918.

[18] Krajnović, S., and Fernandes, J., 2010. "Numerical simulation of the flow around a simplified vehicle model with active flow control, accepted for publication". *Int. J. Heat and Fluid Flow*.

[19] Smagorinsky, J., 1963. "General circulation experiments with the primitive equations". *Monthly Weather Review, 91*(3), pp. 99–165.

[20] Krajnović, S., and Davidson, L., 2002. "Large eddy simulation of the flow around a bluff body". *AIAA Journal, 40*(5), pp. 927–936.
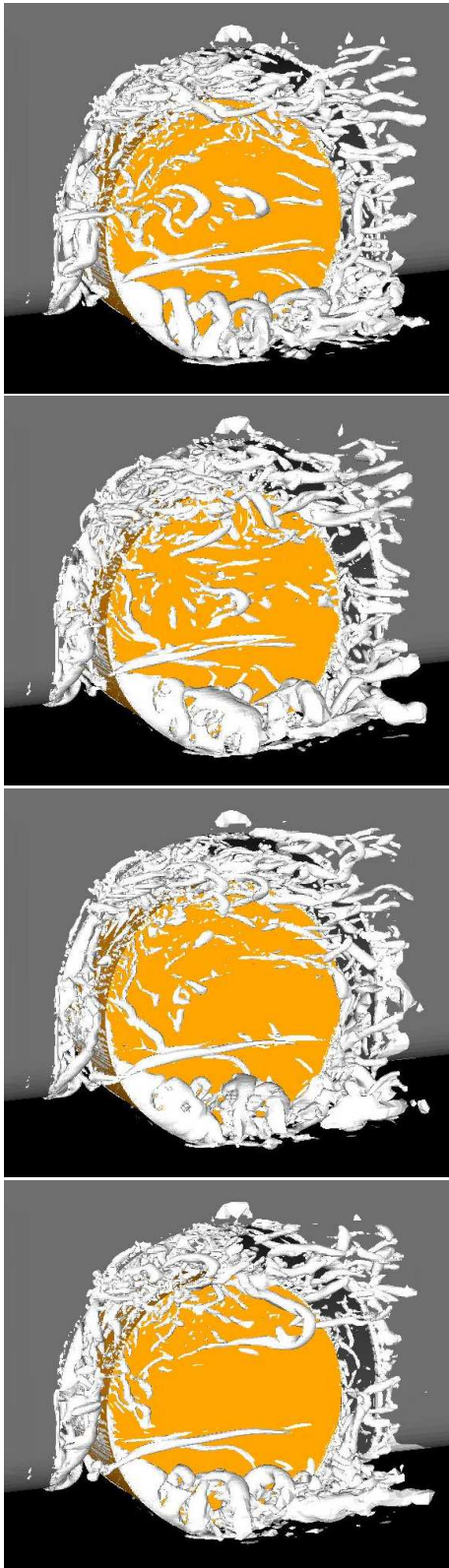
Figure 14. Case 2. Iso-surface of the second invariant of the velocity gradient tensor $Q = 6 \times 10^6$. The time difference between the two picures is $t = 0.04$ or $tU_\infty/D = 0.157$, where D is the diameter of the wheel
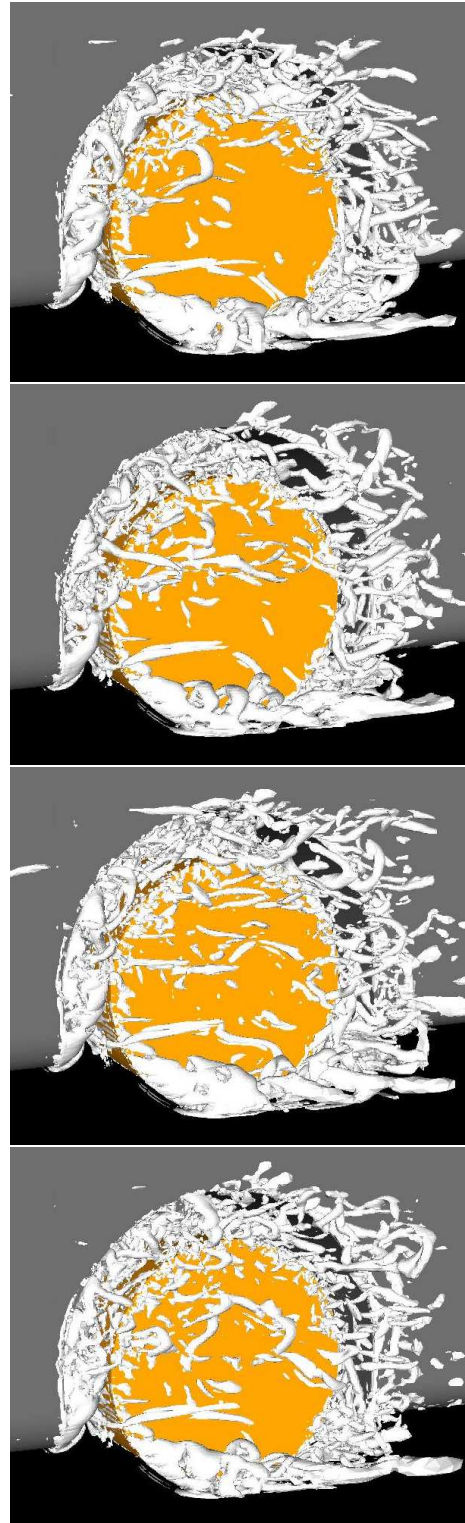
Figure 15. Case 1. Iso-surface of second invariant of the velocity gradient tensor $Q = 6 \times 10^6$. The time difference between the two picures is $t = 0.04$ or $tU_\infty/D = 0.157$, where D is diameter of the wheel